The Goldstone Interferometer for Earth Physics

J. L. Fanselow, P. F. MacDoran, J. B. Thomas, and J. G. Williams
Tracking and Orbit Determination Section

C. J. Finnie and T. Sato
Communications Elements Research Section

L. Skjerve
Philco-Ford Corporation

D. J. Spitzmesser
DSIF Operations Section

The first in a series of very long baseline interferometry feasibility demonstrations for applications to Earth Physics was conducted on January 29, 1971. In this demonstration two Goldstone tracking stations, the 26-m Echo station and the 64-m Mars station, were equipped with JPL hydrogen maser frequency systems and operated in electrically independent, although coordinated, observing modes. S-band (2.3 GHz) radio signals from 14 celestial radio sources were recorded at each station on digital magnetic tape. Later, these tapes were brought together for computer cross-correlation to produce an interferometric observable. Using the interferometer fringe frequency, a measurement of the two equatorial baseline components was made. The discrepancy between these measurements and the inter-station geodetic survey was less than 30 cm in each of these two components.

I. Introduction

In very long baseline interferometry (VLBI) measurements, the radio signal produced by a distant source is recorded simultaneously at two radio antennas. Because of a difference in raypaths, the signal will be delayed in time at one antenna relative to the other. By cross-correlating the two signals, the time delay and/or its time derivative may be determined. When narrow band recording equipment is used, as in the present work, only the time derivative of the time delay may be measured with adequate precision to be useful. If the radio signal is generated by an extragalactic object, the radio source may be regarded as a fixed object because of its great distance.

In this case, the time variation of the time delay is due entirely to the Earth's motion, but depends, of course, on the source location and the baseline vector between the two antennas. In general, measurement of the derivative of the time delay for many natural sources can lead, by means of a least-squares analysis, to the determination of source locations, the baseline vector, and Earth motion parameters, such as UT1 (Universal Time), and polar motion.

The VLBI Earth Physics Program at JPL has established among its goals the measurement of UT1, polar motion, and baseline vectors with submeter accuracy. The first experiment in this program was a feasibility demonstration conducted on January 29, 1971, between the 26-m Echo station and the 64-m Mars station of the Goldstone Deep Space Communications Complex (see Fig. 1). Although the stations were separated by only 16 km, the instrumentation of each station was electrically independent from that of the other. Such independence is of primary importance to the technique of VLBI and therefore makes this experiment a meaningful precursor to future VLBI Earth Physics experiments with overseas Deep Space Network (DSN) stations. The shortness of the Goldstone baseline afforded several advantages for a first experiment. Specifically, the reduced sensitivity to transmission media effects, source position errors, universal time, polar motion, and logistical support simplified the perfection of observing techniques and the development of data reduction software.

This article outlines narrowband interferometer theory, summarizes these short baseline experiments, and presents the results of these measurements.

II. Experiment Description

One of the main considerations in the design of this first feasibility demonstration was to make maximum use of existing DSN station resources. D. S. Robertson and A. H. Legg of the Weapons Research Establishment, Australia, had previously developed a VLBI recording method using the Digital Instrumentation Subsystem (DIS), which is a part of every DSN station. The recorded bandwidth was 24 kHz, dictated primarily by the DIS tape recorders. A discussion of this recording method may be found in Ref. 1, although Fig. 2 of this article contains the most salient features of the configuration used.

In this configuration each station was electrically independent of the other except for a voice circuit used for observing coordination. In effect, the separation of the stations could have been arbitrarily large, specifically intercontinental. The use of hydrogen maser frequency systems to control the receiver local oscillators at these isolated stations provided a level of precision previously unattainable by more conventional frequency standards.

Radio noise from 14 celestial sources was observed at S-band (2298 MHz). Forty pairs of magnetic tapes, each of 12 minutes duration, were recorded in a series of observations spanning ± 60 deg of local hour angle and $+67$ to -43 deg of declination between 20:00 GMT, January 29, 1971, and 07:00 GMT, January 30, 1971. Table 1 summarizes the specific sources used for this experiment.

III. Interferometry Theory (Narrow Band)

Figure 3 shows a schematic diagram of a radio interferometer station pair, while Fig. 4 gives the geometry of the situation. Since these two antennas are separated by a distance $|\mathbf{D}|$, there will be a difference in the time of reception of the signal at the two antennas. This delay, τ_g, is given by

$$\tau_g = \frac{\mathbf{D}}{c} \cdot \hat{\mathbf{s}} \tag{1}$$

where c is the speed of light, and $\hat{\mathbf{s}}$ is a unit vector opposite the direction of propagation of the wave front (assumed plane for simplicity only). This time delay has a maximum possible value of the Earth's radius/c, or 0.021 s. The quantity

$$\nu_F = \omega_0 \frac{\partial \tau_g}{\partial t} \tag{2}$$

is known as the fringe rate, where ω_0 is the received frequency, and is just the negative of the doppler shift between the two stations. In general, cross-correlation of the two data streams allows the time delay τ_g and the fringe rate ν_F to be measured.

The dot product in Eq. (1) is most usefully expanded in terms of the equatorial coordinate system of date. In this system, the right ascension and declination of the source are given by α_s, δ_s while the equivalent quantities for the baseline vector $\mathbf{D}$ are α_b, δ_b.

Explicitly writing out the dot product in Eq. (1),

$$\begin{aligned}\tau_g &= \frac{|\mathbf{D}|}{c}[\cos\delta_b \cos\alpha_b \cos\delta_s \cos\alpha_s \\ &\quad + \cos\delta_b \sin\alpha_b \cos\delta_s \sin\alpha_s + \sin\delta_b \sin\delta_s] \\ &= \frac{|\mathbf{D}|}{c}[\sin\delta_b \sin\delta_s + \cos\delta_b \cos\delta_s \cos(\alpha_b - \alpha_s)]\end{aligned} \tag{3}$$

The fringe rate (2) is then

$$\nu_F = -\frac{|\mathbf{D}|\,\omega_0}{c}\left[\cos\delta_b \cos\delta_s \sin(\alpha_b - \alpha_s)\right]\frac{\partial}{\partial t}(\alpha_b - \alpha_s) \tag{4}$$

If the equatorial projection of $|\mathbf{D}|$ is called r_b,

$$r_b = |\mathbf{D}| \cos\delta_b \tag{5}$$

Since

$$\frac{\partial}{\partial t}(\alpha_b - \alpha_s) = \omega_e \tag{6}$$

where ω_e is the angular velocity of rotation of the Earth (0.73×10^{-4} rad/s),

$$\nu_F = \frac{\omega_0 r_b}{c}\,\omega_e \cos\delta_s \sin(\alpha_b - \alpha_s) \tag{7}$$

Equation (3) emphasizes that cylindrical coordinates are the natural units for this problem. However, the problem is also conveniently expressed in terms of a right-handed cartesian coordinate system fastened to the Earth with the x axis through Greenwich and the z axis along the instantaneous rotation axis. If $\alpha_G(t)$ is the right ascension of Greenwich, and λ_b is the longitude of the baseline in the Earth-fixed system, then

$$\lambda_b = \tan^{-1}\left(\frac{y_2 - y_1}{x_2 - x_1}\right) \tag{8}$$

where x_i, y_i, z_i refer to the Earth-fixed, geocentric coordinates of the ith station, and the right ascension of the baseline vector becomes

$$\alpha_b(t) = \lambda_b + \alpha_G(t) \tag{9}$$

In a system fixed to the Earth,

$$X = |\mathbf{D}| \cos\delta_b \cos\lambda_b \tag{10}$$

$$Y = |\mathbf{D}| \cos\delta_b \sin\lambda_b \tag{11}$$

$$Z = |\mathbf{D}| \sin\delta_b$$

where X, Y, Z are the projections of the baseline on the x, y, z axes. The geometry of the Goldstone baseline is illustrated in Fig. 5.

Substituting Eq. (9) into Eq. (3), one can obtain

$$\tau_g = \frac{1}{c}\left(Z \sin\delta_s + \cos\delta_s \left\{X \cos\left[\alpha_G(t) - \alpha_s\right] - Y \sin\left[\alpha_G(t) - \alpha_s\right]\right\}\right) \tag{12}$$

and

$$\nu_F = -\frac{\omega_e \omega_0}{c}\left(\cos\delta_s \left\{X \sin\left[\alpha_G(t) - \alpha_s\right] + Y \cos\left[\alpha_G(t) - \alpha_s\right]\right\}\right) \tag{13}$$

Because of the narrow recorded bandwidth (24 kHz) of this experiment, the time delay observable (τ_g) was restricted in precision to a few microseconds (1 μs = 300 m). This experiment was aimed at making baseline measurements with submeter accuracy. Therefore, the time delay was ignored in favor of the fringe frequency observable which could provide the required precision. Since the fringe frequency is independent of z as indicated by Eq. (13), these measurements could precisely determine only the equatorial projection of the baseline.

Because we are interested in only the phase and frequency of the cross-correlation function, it is necessary only to analyze the interferometer response to monochromatic illumination.

Although the video signals at each station are infinitely clipped and digitally recorded, an analog derivation of the signal recording and processing contains the essential features of the technique.

Suppose that the electric field detected at antenna 1 is given by the expression

$$E_1(t) = E_0 \cos\left[\omega_0 t + \phi_{T1}(t)\right] \tag{14}$$

where ω_0 is the frequency at S-band, and ϕ_{T1} represents the phase drift due to transmission media. The retarded field detected at station 2 will then become

$$E_2(t) = E_0 \cos\left[\omega_0 (t - \tau_g) + \phi_{T2}(t)\right] \tag{15}$$

where τ_g represents the differential time of arrival due to the geometry and ϕ_{T2} represents the transmission media effects along the raypath to station 2. The voltage signal recorded at antenna 1 may be represented by the expression

$$V_1(t) = A \cos\left[(\omega_0 - \omega_1)\, t + \phi_{T1}(t) + \phi_{I1}(t)\right] \tag{16}$$

where ω_1 is the effective mixing frequency and ϕ_{I1} represents instrumental phase shifts. Similarly, the recorded signal at antenna 2 is given by the expression

$$V_2(t) = A\cos[(\omega_0 - \omega_2)t - \omega_0\tau_g + \phi_{T2}(t) + \phi_{I2}(t)] \quad (17)$$

IV. Data Reduction

In the cross-correlation process, the signal from station 2 is offset by a model time delay τ_m, and the two signals are multiplied together in order to produce a beat signal of the form

$$\begin{aligned} F(t) &= V_1(t)\,V_2(t+\tau_m) \\ &= A\cos[(\omega_2 - \omega_1)t + \omega_2\tau_m \\ &\quad + \omega_0(\tau_g - \tau_m) + \phi_I(t) + \phi_T(t)] \end{aligned} \quad (18)$$

where

$$\phi_I = \phi_{I1} - \phi_{I2}$$

$$\phi_T = \phi_{T1} - \phi_{T2}$$

The model time delay τ_m is calculated on the basis of an assumed baseline and source location.

For efficiency in data handling, the beat signal $F(t)$ (fast fringes) is digitally processed to remove the known higher frequency components of the phase. This procedure, which is called fringe stopping, is analogous to the heterodyne function of a receiver using a heterodyne frequency of $(\omega_2 - \omega_1) + \omega_2\dot{\tau}_m$. The stopped fringes G_S are given by

$$G_S(t) = A\cos[\omega_0(\tau_g - \tau_m) + \phi_T(t) + \phi_I(t)] \quad (19)$$

An example of stopped fringes is shown in Fig. 6 along with a cosine curve fit to them by least squares. Because of the $2\pi n$ ambiguity involved in inversion of trigonometric functions, only the time dependence of the phase may be obtained from the stopped fringes. That is, the phase may be determined except for an unknown additive constant. Two methods are presently used to extract this time dependence: Fourier analysis and phase tracking.

The first method, Fourier analysis, is useful when the stopped fringe frequency is effectively constant over the integration period. The choice of integration period T depends on the instrumental stability, transmission media stability, and time delay modelling accuracy. A Fourier transform of the stopped fringes yields the stopped fringe frequency ν_S, which is given by

$$\nu_S = \text{stopped fringe frequency} = \nu_R + \nu_N \quad (20)$$

where

$$\nu_N = \text{frequency offset} = \dot{\phi}_I + \dot{\phi}_T \quad (21)$$

$$\nu_R = \text{residual fringe frequency} = \omega_0(\dot{\tau}_g - \dot{\tau}_m) \quad (22)$$

The term ν_R is called the *residual fringe frequency*, whereas the quantity ν_N is called the *frequency offset* and is intended as a general term. As indicated above, it results from the combined effects of instrumental and transmission media phase shifts. For this experiment, the simplest model for ν_N assumes $\dot{\phi}_T = 0$ and $\dot{\phi}_I =$ constant, the latter accounting for an offset between the two first local oscillator frequencies. As will be discussed later, ν_N actually was not constant during certain portions of the experiment.

Figure 7 displays the Fourier transform of one of the short baseline runs with an integration time T of approximately 700 s. The transform of a single frequency is proportional to $[\sin(T\Delta\nu/2)]/(T\Delta\nu/2)$, where $\Delta\nu$ is the frequency difference from ν_S and has a half-width to the first null of $1/T$. Since Fig. 7 exhibits this expected shape, a narrow range of frequencies (< 0.2 mHz) is present in the fringe rate. The upper limit is consistent with expected hydrogen maser performance and expected modelling accuracy.

Although the Fourier transform technique can efficiently extract the stopped fringe frequency and reveal spectral distributions that are comparable to the natural $1/T$ width of the Fourier transform, it cannot reveal the time history of phase excursions which could be useful in data interpretation. Therefore, a least-squares technique was used to count cycles in order to determine the time dependence of the phase. The initial phase of individual 33-s segments is obtained by the data fitting technique illustrated in Fig. 6. In this manner, 21 initial phase values were calculated for each 700-s run, thereby giving the time dependence of the phase. These 21 phase values were then fit by a least-squares linear time function over the tape length (700 s). The slope of this fit function is equal to the (average) stopped fringe frequency for that run. Phase residuals are obtained by subtracting from each individual phase value the corresponding linear fit value. Figures 8a and 8b show phase residuals for runs 15 and 20. Phase residuals produced by the linear fit will be random if no systematic nonlinear trends are present in the phase because of modelling error, instrumental instability or transmission media. For the present short baseline experiment, a model time delay can be constructed that is accurate enough to make the residual fringe frequency

change undetectable over a 700-s interval. Thus, in this particular experiment, nonlinear phase excursions indicate instrumental or transmission media phase drifts. Figure 8a consists mainly of random noise and indicates a frequency stability better than 50 μHz at S-band or $\Delta f/f \lesssim 2 \times 10^{-14}$. Figure 8b, however, seems to contain systematic phase deviations of the order of 0.1 cycle and indicates that the frequency (instantaneous slope) wanders by about 1 mHz. Further investigation is required to determine whether these short-term excursions are produced by instrumental instability or by the transmission media.

Random residuals that appear in the residual phase plots appear to be due primarily to receiver noise and lead to frequency measurement errors in the 20- to 200-μHz range for correlated source strengths of 1 to 10 flux units[1] and integration times of 700 s. H-maser flicker noise can contribute an additional uncertainty between 15 to 30 μHz at S-band. Thus, the inherent accuracy of the narrow-band system should fall in the 20- to 200-μHz range for S-band measurements for sources with 1–10 flux units of unresolved power. Such frequency accuracy in principle would allow baseline measurements with an uncertainty between 5 and 30 cm. However, instrumental and transmission media phase excursions often prohibit measurements of this accuracy. For example, calibration or control of the 1-mHz frequency variations revealed in the NRAO 190 plot (Fig. 8b) will be necessary in order to exploit the inherent accuracy of the interferometer.

V. Stopped Fringe Frequency Model

After cross-correlation and fringe analysis, the reduced data consist of a stopped fringe frequency for each run. Since the model for the time delay was only approximate, the fringe rate after stopping is not zero. Therefore, an additional model must be constructed for the stopped fringe frequency in order to extract the actual baseline. As seen in Eq. (20), the stopped fringe frequency is given by

$$\nu_S = \omega_0 (\dot{\tau}_g - \dot{\tau}_m) + \dot{\phi}_T + \dot{\phi}_I \tag{23}$$

where the first term represents the residual fringe frequency and $\dot{\phi}_T$ and $\dot{\phi}_I$ are the time derivatives of the transmission media and instrumental phase drifts.

In general, the residual fringe frequency can be due to several errors in the model time delay. However, in the short baseline experiment, model errors due to source locations, UT1, precession, nutation, aberration, and polar motion make contributions to the residual fringe frequency which are below the measurement uncertainty of 50 μHz. Since all of these errors can be represented by an equivalent source position error, their importance may be demonstrated by evaluating the partial derivatives of the fringe frequency, Eq. (7), with respect to the source angles α_s and δ_s:

$$\frac{\partial \nu_F}{\partial \alpha_s} = \frac{\omega_0 \omega_e r_b}{c} \cos \delta_s \cos (\alpha_b - \alpha_s) \tag{24}$$

$$\frac{\partial \nu_F}{\partial \delta_s} = -\frac{\omega_0 \omega_e r_b}{c} \sin \delta_s \sin (\alpha_b - \alpha_s) \tag{25}$$

For both derivatives, the maximum sensitivity for the Goldstone baseline is 30 μHz/arc sec. Since the aggregate effect of all the above error sources was equivalent to less than one arc sec in source position, their combined contribution to the residual fringe frequency was less than 30 μHz. Thus, the residual fringe frequency model must only account for baseline error and is given by

$$\omega_0 (\dot{\tau}_g - \dot{\tau}_m) = \frac{\partial \nu_F}{\partial X} \Delta X + \frac{\partial \nu_F}{\partial Y} \Delta Y \tag{26}$$

where ΔX, ΔY are the corrections to the equatorial components of the baseline and where

$$\frac{\partial \nu_F}{\partial X} = \frac{\omega_0 \omega_e}{c} \cos \delta_s \sin [\alpha_G (t) - \alpha_s] \tag{27}$$

$$\frac{\partial \nu_F}{\partial Y} = -\frac{\omega_0 \omega_e}{c} \cos \delta_s \cos [\alpha_G (t) - \alpha_s] \tag{28}$$

as indicated by Eq. (13).

Because of the proximity of the raypaths in a short baseline measurement, the transmission media phase shifts along the two paths should be nearly identical so that the difference found in the interferometer phase shift ϕ_T should be nearly zero. If the instrumentation at both stations were perfectly stable but a small offset existed between the two local oscillators, the instrumental term $\dot{\phi}_I$ would be constant. Under these conditions, the frequency offset ν_N could be represented by a constant.

Under all of these assumptions, the fitting equations become

[1]One flux unit = 10^{-26} watts/m^2/Hz. Table 1 lists flux measurements on 10 sources using the DSS 14 total power radiometer.

$$\left.\begin{aligned} \nu_1 &= \left.\frac{\partial \nu_F}{\partial X}\right|_1 \Delta X + \left.\frac{\partial \nu_F}{\partial Y}\right|_1 \Delta Y + \nu_N \\ \nu_2 &= \left.\frac{\partial \nu_F}{\partial X}\right|_2 \Delta X + \left.\frac{\partial \nu_F}{\partial Y}\right|_2 \Delta Y + \nu_N \\ &\vdots \\ \nu_i &= \left.\frac{\partial \nu_F}{\partial X}\right|_i \Delta X + \left.\frac{\partial \nu_F}{\partial Y}\right|_i \Delta Y + \nu_N \end{aligned}\right\} \quad (29)$$

where ν_i is the stopped fringe frequency for the ith run, ν_N is a constant frequency offset, and ΔX, ΔY are corrections to the assumed equatorial components of the baseline. The partials are evaluated at the middle of the run interval.

VI. Results

From a total set of 40 runs, 33 tape pairs were readily processed. Seven pairs were deleted primarily because of tape writing problems. When the stopped fringe frequencies for these 33 runs were simultaneously fit by least-squares using the model of the previous section, the rms residual for the total set was 500 μHz. These fit residuals were obtained by subtracting the right-hand side of Eq. (29) (using the fit values for ΔX, ΔY, and ν_N) from the observed stopped fringe frequency for each run. Such large residuals were in sharp contrast with the typical measurement uncertainty of 50 μHz for individual runs.

This disagreement forced a reappraisal of all the assumptions used in the data reduction. One of the assumptions involved the constancy of the frequency offset ν_N. To test the possibility of temporal variations in ν_N, we assumed that the frequency offset experienced long-term variations but was constant during certain unknown time intervals. The advantage of this hypothesis was that the above model could be applied during any time interval suspected of constant offset. The 33 runs were separated into various sequences and each segment was fit separately using the constant offset model. Most sequences produced large residuals ($\approx 500\,\mu$Hz) and baseline corrections that disagreed between sequences by as much as 5 meters. However, we were able to locate two time intervals for which the fit residuals were small ($< 100\,\mu$Hz) and for which the baseline corrections were in agreement.

Table 2 summarizes these results in terms of the baseline corrections (ΔX, ΔY), frequency offset ν_N, and fit residuals. The errors in the table are one standard deviation formal statistical errors. Figure 9 illustrates the stopped fringe frequency values obtained for runs 26–40 and the fit residuals for these runs. Both the small residuals and the baseline agreement between the two sequences indicate that the assumption of a constant frequency offset during each of these two sequences is valid.

When the results for these two sequences are combined, they yield the following baseline corrections:

$$\Delta X = 1.2 \pm 0.2\,\text{m}$$

$$\Delta Y = 0.3 \pm 0.3\,\text{m}$$

The final adopted errors have been made larger than the formal statistical errors in an attempt to account for systematic trends in the residuals.

The full corrected equatorial baseline components are obtained by applying the above composite baseline corrections to the assumed baseline as shown in Table 3. Geodetic survey values (Ref. 2) have also been included in this table and are in excellent agreement with the interferometer results.

If we assume that the measured baseline corrections are valid, the frequency offset for each run may be obtained by subtracting the residual frequency due to this baseline error from the stopped fringe frequency. This has the same effect as repeating the cross-correlation and fringe stopping procedures using the corrected baseline. The resulting frequency offsets are plotted versus run number and time in Fig. 10. The plot indicates that the offset exhibited 1-mHz excursions relative to the nighttime value.

VII. Discussion

Unexplained frequency and phase excursions were present with both short-term (minutes) and long-term (hours) variations. The source of the variations could conceivably be either transmission media or instrumentation.

Consider first the short-term variations of which Fig. 8b is an example. In that case, a 0.2 S-band cycle drift occurs, implying a 2.6-cm phase change. It is not possible to uniquely identify the source of these excursions; however, some physical mechanisms can be hypothesized which produce similar effects. For example, the troposphere represents a 2.2-m phase delay at the zenith. Thus, only about a 1% difference is needed in the raypaths to cause a 2.6-cm phase shift. A similar argument applies for the effects on the ionosphere. While the transmission media is a possible cause, instrumental phase shifts of 2.6 cm are also possible.

The long-term variations are seen in Fig. 10. One of the most obvious features of Fig. 10 is the apparent frequency offset dependence on time of day. A day versus night dependence connotes a thermal heating or transmission media effect, particularly the ionosphere.

In order for the transmission media to be the cause of the Fig. 10 excursions, the observations must exhibit some particular properties. For example, there should be some dependence on the elevation angle of the antennas and the magnitude of the effects must be consistent with likely dissimilarities in the two raypaths, since an interferometer is inherently a differential device.

Figure 11 shows the tropospheric frequency error for a single raypath versus run number, given a 2.2-m zenith phase delay. This figure accounts for no transmission media cancellation due to the similarity of the raypaths and is therefore the worst-case error. With regard to the magnitude of the frequency excursions in Fig. 10, it seems unlikely that 2-mHz tropospheric effects could be introduced differentially in the interferometer raypaths. In addition, a comparison of Figs. 10 and 11 shows virtually no correlation. For these reasons, the troposphere may be rejected as a cause of the long-term offset variations.

By an argument similar to the one given above, the ionosphere also becomes a doubtful source of these long-term variations.

If the frequency offset variations are due solely to instrumental instability, a time integration of the frequency offset (Fig. 10) will yield the long-term instrumental phase excursions. By taking the nighttime offset as base frequency and arbitrarily making the phase zero at 12:00 local time, one can integrate the offset to obtain the phase excursions shown in Fig. 12. The phase increased to about 7 cycles by 15:00 local time and then decreased to -5 cycles at 20:00 and remained essentially constant until the end of the experiment, 23:00.

The major instrumental elements to be suspected are the frequency synthesizers, traveling-wave S-band maser, hydrogen maser frequency system, and antenna cabling. Preliminary investigations conducted at the Goldstone DSCC[2] have shown cable electrical length stabilities of 0.01 cycle of S-band except during periods of rapid thermal changes, such as sunrise. The sunrise heating has been observed to result in 0.1-cycle shift within about one-half hour. Thus, the largest phase rates expected would be 50 μHz and then only in a transient manner. Frequency offsetting mechanisms to explain Fig. 10 must be sustainable at the millihertz level over hours.

[2]Personal communications with F. Borncamp, DSIF Operations Section, JPL.

Frequency variations originating in the H-maser output are highly unlikely at the part in 10^{12} level that would be required for millihertz variations at S-band, making the H-masers an unlikely source of the excursions.

The traveling-wave maser (TWM) operates at S-band and provides the first stage of amplification for each station. A TWM is constructed in such a way that hundreds of wavelengths are present within its slow wave structure. Since changes in the observed frequency offset of Fig. 10 could have been caused by changes in electrical path, the TWM was a suspect component. The effects of temperature, magnetic field strength, and magnetic field shape have been examined and reported in Ref. 3. The electrical path length changes (<18 deg) measured in that work were far from the 12-cycle shifts required by Fig. 12. TWM phase shifts have been observed due to the Earth's magnetic field. However, R. C. Clauss[3] reports that tests conducted at DSS 14 showed 30-deg phase shifts with an azimuthal dependence. Thus, the TWM does not appear to be the cause of the frequency offset variations.

The last major instrumental suspect is the Hewlett Packard model 5100B frequency synthesizers. As seen in Fig. 2, four synthesizers were used in each station's configuration. The interferometer is sensitive to the performance of all the synthesizers but is particularly sensitive to the synthesizer used to generate the first local oscillator signal since instabilities in this first local oscillator synthesizer are multiplied by 96. Table 2 and Fig. 11 show that the baseline solution for runs 26–40 generated an rms residual of 74 μHz, indicating a fractional frequency deviation of not greater than $\Delta f/f = 3 \times 10^{-14}$ over time spans of 10 minutes to 4 hours during these last 13 runs.

Performance specifications for the synthesizer are not stated by Hewlett Packard for averaging times greater than 1 second, where it is $\Delta f/f = 1 \times 10^{-11}$. Under the most ideal circumstances (white phase noise), the synthesizer's fractional frequency deviation could improve only by the square root of the averaging time. Therefore, at 10 minutes, the performance should be about $\Delta f/f = 4 \times 10^{-13}$. The frequency system performance achieved on runs 26–40 was an order of magnitude better than could be inferred from the manufacturer's specified performance. Thus, the data indicates that the synthesizers did outperform inferred specifications during certain periods; however, it is also possible that the long-term performance was at the part in 10^{12} level, giving rise to the observed frequency offset variations of Fig. 10.

[3]Communications Elements Research Section, JPL.

VIII. Summary

Independent station radio interferometry has been used to measure the baseline between two stations of the Goldstone Deep Space Communications Complex with an accuracy of 30 cm. This short baseline experiment has revealed long-term (hours) and short-term (minutes) frequency instabilities that require either calibration or control before the inherent accuracy of less than 10 cm can be achieved. The experience of this interferometer demonstration has allowed the development of observing techniques, data reduction software, and results which could be independently verified with high precision.

References

1. Sato, T., Skjerve, L., and Spitzmesser, D., "Radio Science Support," in *The Deep Space Network*, Space Programs Summary 37-62, Vol. II, pp. 125–127. Jet Propulsion Laboratory, Pasadena, Calif., Mar. 31, 1970.
2. Mulhall, B. D., et al., *Tracking System Analytic Calibration Activities for the Mariner Mars 1969 Mission*, Technical Report 32-1499. Jet Propulsion Laboratory, Pasadena, Calif., Nov. 15, 1970.
3. Clauss, R. C., "Low-Noise Receivers, Microwave Maser Development, Second Generation Maser," in *The Deep Space Network*, Space Programs Summary 37-51, Vol. II, pp. 73–77. Jet Propulsion Laboratory, Pasadena, Calif., May 31, 1968.

Table 1. Summary of radio sources used in short baseline experiment

Source	Position						Number of runs	Observed total flux density[a] (Jan. 29, 1971), flux units
	Right ascension (1950.0)			Declination (1950.0)				
	Hour	Min	Second	Degree	Min	Second		
P 0106 + 01[b]	01	06	04.54	01	19	00.3	4	1.8 (2)[c]
DW 0224 + 67	02	24	43.	67	07	35.	1	
P 0237 − 23[b]	02	37	52.75	−23	22	05.9	4	5.6 (2)
3C 84[b]	03	16	29.526	41	19	52.78	4	12.0 (1)
NRAO 140[b]	03	33	22.38	32	08	36.8	3	3.0 (1)
3C 120[b]	04	30	31.63	05	14	59.5	4	5.8 (2)
P 0438 − 43[b]	04	38	44.	−43	38	51.	1	9.2 (1)
NRAO 190[b]	04	40	05.29	−00	23	20.1	6	3.0 (3)
P 0521 − 36	05	21	13.00	−36	30	15.	1	13.1 (1)
3C 345	16	41	17.56	39	54	10.6	3	
P 1741 − 038	17	41	20.60	−03	48	49.0	1	
P 2134 + 004	21	34	05.29	00	28	25.8	1	
CTA 102[b]	22	30	07.80	11	28	22.8	3	5.2 (1)
3C 454.3[b]	22	51	29.52	15	52	53.7	4	11.5 (2)

[a]20% uncertainty.
[b]Denotes sources used for baseline solution.
[c]Number of measurements in parentheses.

Table 2. Interferometer-derived corrections to assumed baseline

Runs	ΔX, m	ΔY, m	ν_N, mHz	Rms residual, μHz
15–23	0.9 ± 0.35	−0.23 ± 0.2	2.56 ± 0.1	95
26–40	1.4 ± 0.15	−0.47 ± 0.3	3.6 ± 0.2	74

Table 3. Equatorial baseline components

Baseline	X, m	Y, m	r_b, m	λ_b, deg
Assumed	−3179.6	10637.2	11102.2	163.3578
Corrected	−3178.4 ± 0.2	10636.9 ± 0.3	11101.6 ± 0.3	163.3633 ± 0.0011
Surveyed	−3178.42 ± 0.15	10636.60 ± 0.15	11101.3 ± 0.16	163.3628 ± 0.0007

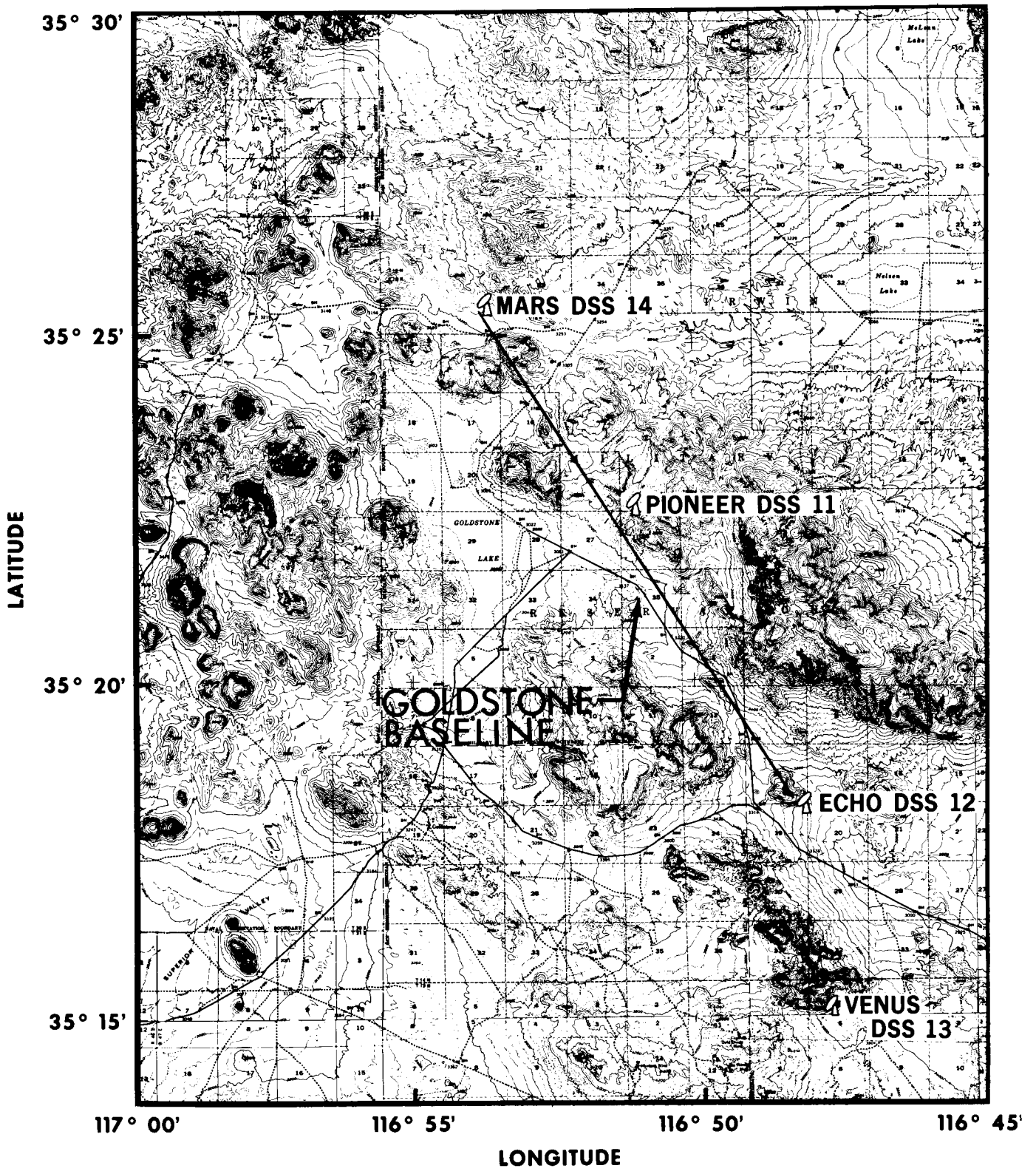

Fig. 1. Goldstone Deep Space Communications Complex

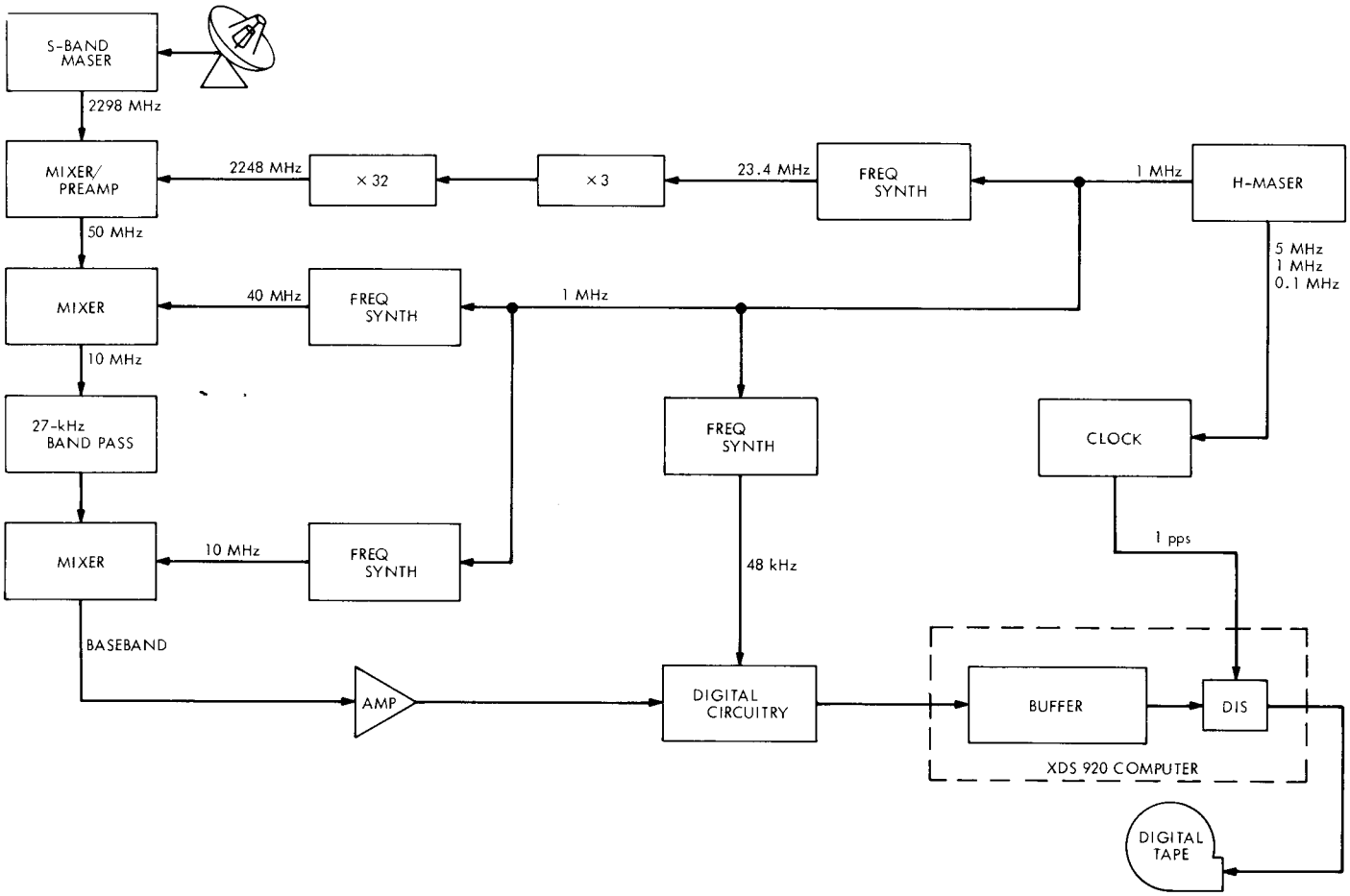

Fig. 2. Interferometry station configurations

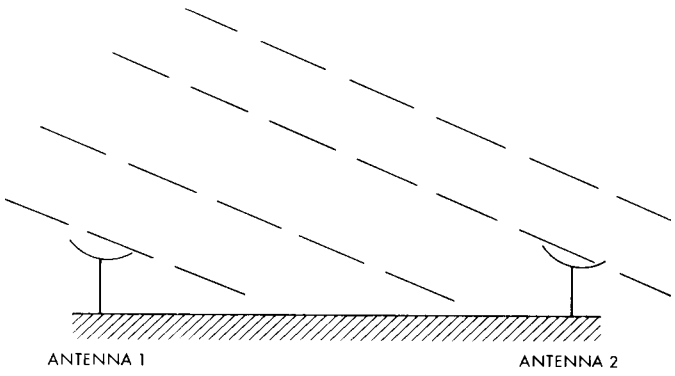

Fig. 3. Interferometer pair

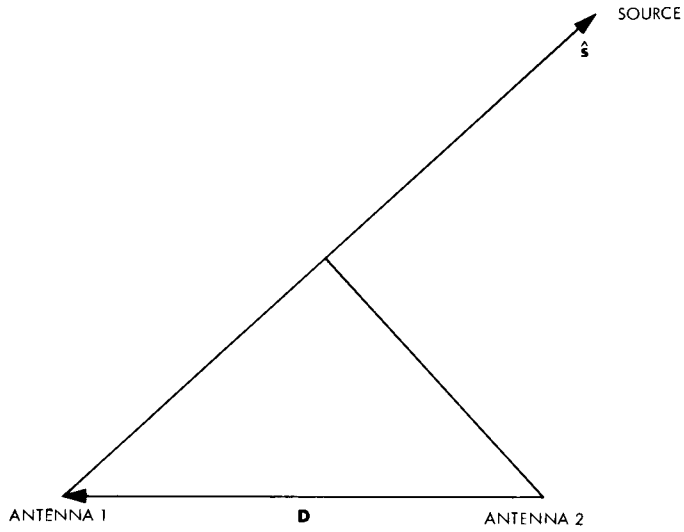

Fig. 4. Interferometer geometry

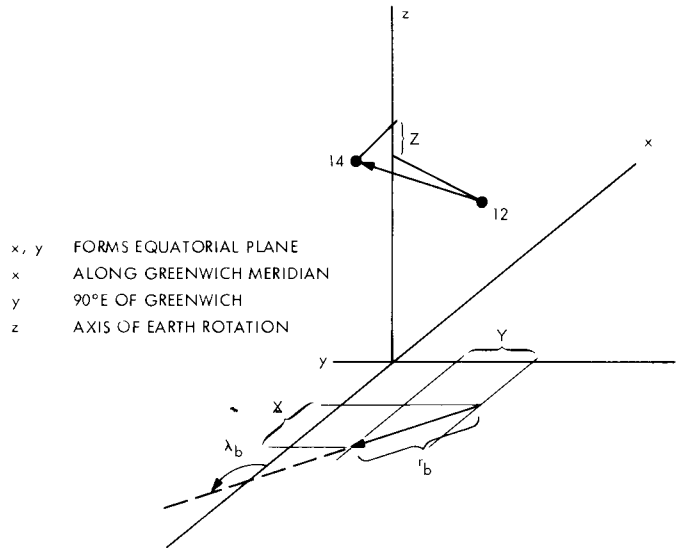

Fig. 5. Goldstone (DSS 12, 14) baseline

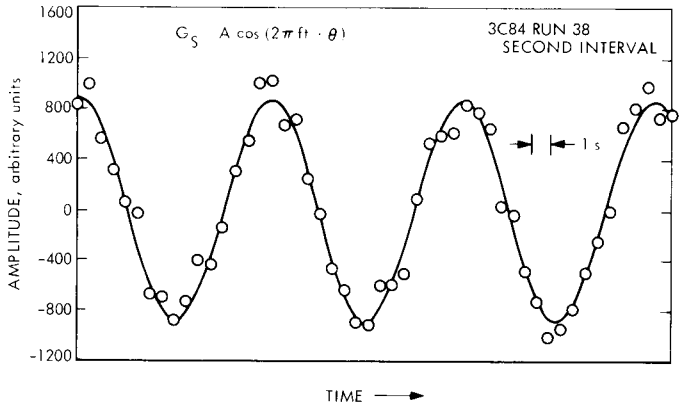

Fig. 6. Stopped fringes

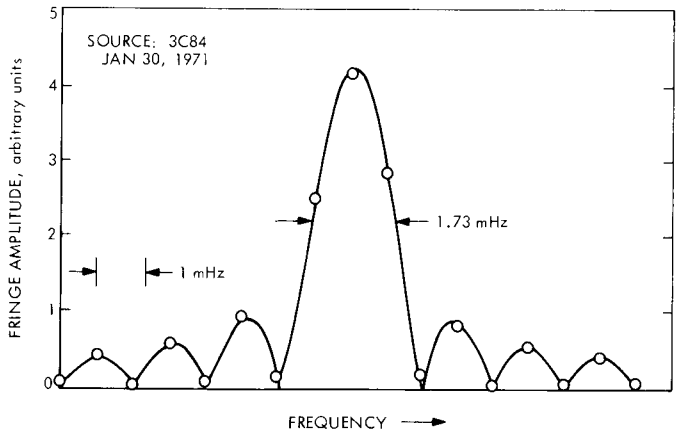

Fig. 7. Fourier transform of residual fringes

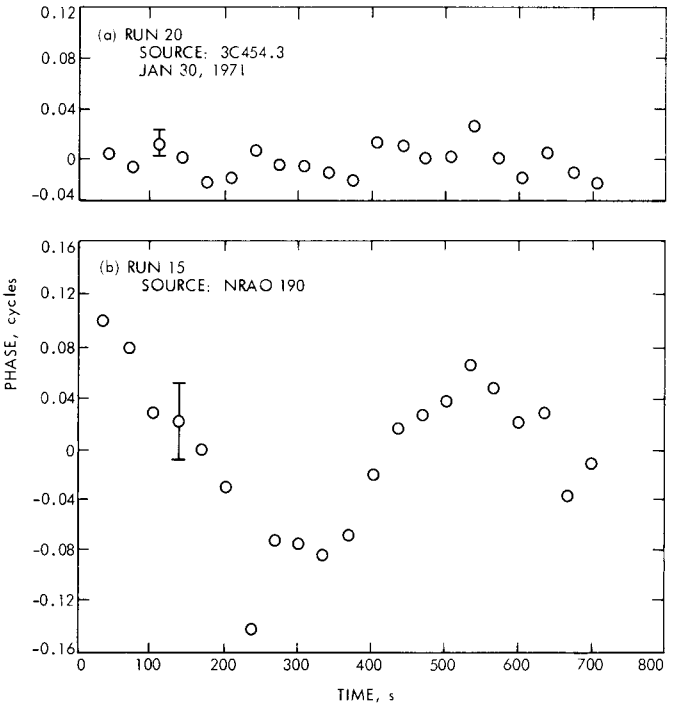

Fig. 8. Fringe phase residuals

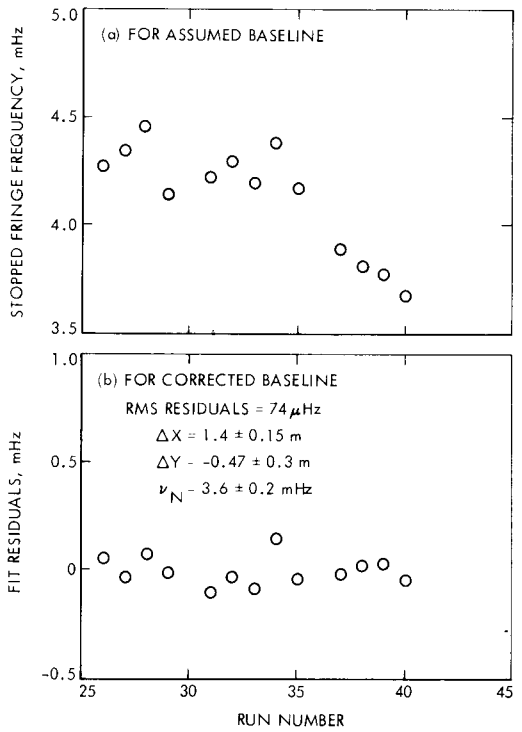

Fig. 9. Stopped fringe frequency values and fit residuals for runs 26–40

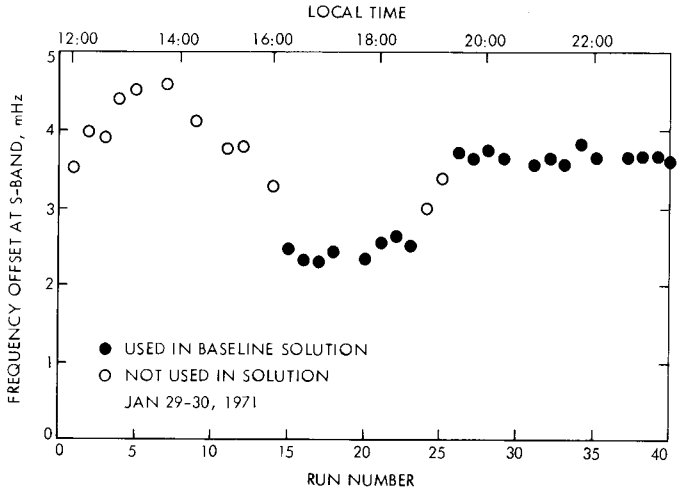

Fig. 10. Interferometer frequency offset for corrected baseline

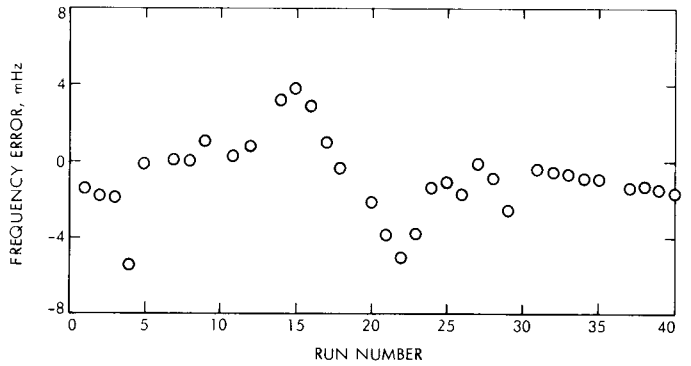

Fig. 11. Tropospheric frequency error for a single raypath

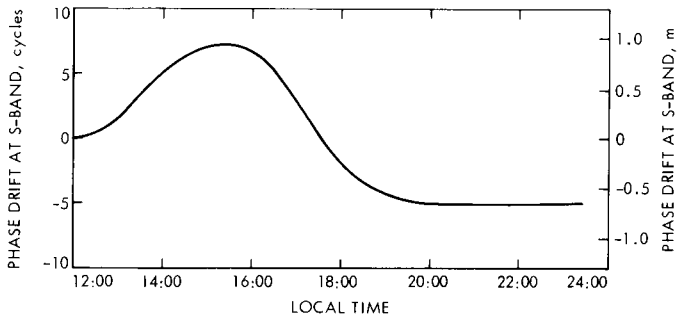

Fig. 12. Interferometer phase drift